Two-magnon raman scattering in a spin density wave antiferromagnet

Friedhelm Schönfeld, Arno P. Kampf, Erwin Müller-Hartmann

Two-magnon Raman scattering in a spin density wave antiferromagnet

Friedhelm Schönfeld, Arno P. Kampf, Erwin Müller-Hartmann

Institut für Theoretische Physik, Universität zu Köln, Zülpicher Strasse 77, D-50937 Köln, Germany
(e-mail: fsch@thp.uni-koeln.de, Tel.: +49-221/470-4208, Fax: +49-221/470-5159)

Abstract. We present the results for a model calculation of resonant two-magnon Raman scattering in a spin density wave (SDW) antiferromagnet. The resonant enhancement of the two-magnon intensity is obtained from a microscopic analysis of the photon-magnon coupling vertex. By combining magnon-magnon interactions with 'triple resonance' phenomena in the vertex function the resulting intensity line shape is found to closely resemble the measured two-magnon Raman signal in antiferromagnetic cuprates. Both, resonant and non-resonant Raman scattering are discussed for the SDW antiferromagnet and a comparison is made to the conventional Loudon-Fleury theory of two-magnon light scattering.

I. Introduction

Soon after the discovery of high-T_c superconductivity [1] Raman scattering experiments were performed on the antiferromagnetic (AF) parent compounds La_2CuO_4 [2, 3] and $YBa_2Cu_3O_6$ [4–6]. The analysis of the two-magnon Raman intensity has proven since to be a valuable tool for probing the collective magnetic excitations in these layered materials. Common to all antiferromagnetic cuprates is a well defined two-magnon peak in the Raman intensity in B_{1g} and a weaker but still significant signal in A_{1g} scattering geometry at a transferred photon frequency near 3000 cm^{-1}. The frequency of the two-magnon peak has allowed an estimate for the unrenormalized AF exchange coupling between the copper spins in the CuO_2 planes of about 136 meV in La_2CuO_4, consistent with results of neutron scattering experiments for the spin wave velocity [7] and for the zone boundary magnon energy [8, 9]. Most of the magnetic properties of AF cuprates are well described by modelling the undoped CuO_2 layers by a spin $\frac{1}{2}$ Heisenberg model on a square lattice. Yet, some anomalous features of the two magnon intensity profile have remained a puzzle: both, the asymmetric and broad lineshape in B_{1g} and the appearance of a two-magnon signal also in A_{1g} and B_{2g} geometry cannot be obtained within the traditional Loudon-Fleury theory for two-magnon Raman scattering [10–12].

Furthermore, two-magnon light scattering in AF cuprates is a resonant phenomenon and the scattering intensity as well as the line shape depend on the incoming photon frequency. The Loudon-Fleury theory is in principle a theory for non-resonant Raman scattering, assuming a phenomenological coupling of the incoming and scattered photons to the localized spins of the antiferromagnet as described by the coupling Hamiltonian

$$H_{L-F} = \sum_{<i,j>} (\mathbf{E}_{inc} \cdot \mathbf{u}_{ij})(\mathbf{E}_{sc} \cdot \mathbf{u}_{ij})(\mathbf{S}_i \cdot \mathbf{S}_j) \qquad (1)$$

where $\mathbf{E}_{inc}$ and $\mathbf{E}_{sc}$ are the electric field vectors for the incoming and scattered photons, and $\mathbf{u}_{ij}$ is a unit vector connecting spin sites i and j [10–12]. However, light scattering experiments on AF cuprate compounds so far have been performed with laser photon frequencies comparable to the charge transfer energy gap of these insulating materials [13, 14]. Therefore, photon induced transitions across the insulating energy gap are the natural origin for the resonant features of the two-magnon signal. A successful theory for resonant two-magnon light scattering must for this reason retain the charge degrees of freedom of the electrons.

Along similar lines as in the recent work of Chubukov and Frenkel [15] we perform a model calculation for a spin density wave AF which allows to explore the resonant enhancement of the two-magnon Raman intensity. We calculate the scattering intensity using a microscopic description for the photon-electron coupling and for the creation of a magnon pair. Final state magnon interactions are included within a diagrammatic formulation based on the half-filled single band Hubbard model. We show that in this framework the frequency dependence of the photon-magnon vertices gives rise to an enhancement of the high energy part of the two-magnon spectrum. Several experimental features are explained as a consequence of the interplay between the two-magnon peak and resonance phenomena of the photon-magnon vertex function.

The paper is organized as follows: In Chap. II we start with a brief review of the spin density wave formalism for

the Hubbard model at half-filling. In Chap. III and IV a detailed description of our diagrammatic approach is given and the basic coupling vertices are calculated. The extension to including final state magnon-magnon interactions is presented in Chap. V. In Chap. VI we evaluate results for the non-resonant case and compare them to the conventional Loudon-Fleury theory. In Chap. VII we explore the experimentally relevant resonant case and calculate the scattering intensity with resonant electron-magnon vertex functions. A discussion of our results and the comparison to the experimental data are presented in Chap. VIII.

II. The spin density wave state

We start from the single band Hubbard model on a square lattice which is assumed to describe the low energy physics of the CuO_2 layers. The Hamiltonian for the Hubbard model in standard notation is given by

$$H = \sum_{\mathbf{k},\sigma} \varepsilon(\mathbf{k}) c_{\mathbf{k}\sigma}^+ c_{\mathbf{k}\sigma} + \frac{U}{N} \sum_{\mathbf{k},\mathbf{l},\mathbf{q}} c_{\mathbf{k}\uparrow}^+ c_{\mathbf{q}-\mathbf{k}\downarrow}^+ c_{\mathbf{q}-\mathbf{l}\downarrow} c_{\mathbf{l}\uparrow} \quad . \tag{2}$$

Here $c_{\mathbf{k}\sigma}^{(+)}$ destroys (creates) an electron with momentum $\mathbf{k}$ and spin $\sigma = \uparrow, \downarrow$. N is the number of lattice sites and U is the on-site Coulomb repulsion. The tight binding dispersion of the square lattice with nearest neighbour hopping only is given by $\varepsilon(\mathbf{k}) = -4t\gamma_{\mathbf{k}}$, where t is the hopping amplitude and $\gamma_{\mathbf{k}} = [\cos(ak_x) + \cos(ak_y)]/2$. Throughout the rest of the paper t and the lattice constant a are set to unity.

At half-filling the nesting property $\varepsilon(\mathbf{k}) = -\varepsilon(\mathbf{k}+\mathbf{Q})$ with $\mathbf{Q} = (\pi, \pi)$ leads to an instability of the Fermi sea of non-interacting electrons towards a commensurate spin density wave ground state with wave vector $\mathbf{Q}$. Following the standard procedure as originally outlined by Schrieffer, Wen, and Zhang [16] we introduce the staggered magnetization M in the SDW ground state $|\psi\rangle$ by:

$$M = \langle\psi|S_{\mathbf{Q}}^z|\psi\rangle = \langle\psi|\frac{1}{2N}\sum_{\mathbf{k},\sigma=\uparrow\downarrow} \sigma c_{\mathbf{k}+\mathbf{Q}\sigma}^+ c_{\mathbf{k}\sigma}|\psi\rangle \tag{3}$$

to linearize the interaction part of the Hamiltonian (2). The resulting Hartree-Fock Hamiltonian is diagonalized by the linear transformation

$$\begin{pmatrix} \gamma_{\mathbf{k}\sigma}^c \\ \gamma_{\mathbf{k}\sigma}^v \end{pmatrix} = \mathbf{U}(\mathbf{k},\sigma) \begin{pmatrix} c_{\mathbf{k}\sigma} \\ c_{\mathbf{k}+\mathbf{Q}\sigma} \end{pmatrix} , \quad \mathbf{U}(\mathbf{k},\sigma) = \begin{pmatrix} u_{\mathbf{k}} & \sigma v_{\mathbf{k}} \\ v_{\mathbf{k}} & -\sigma u_{\mathbf{k}} \end{pmatrix} \tag{4}$$

which leads to

$$H = \sum_{\mathbf{k},\sigma}{}' E(\mathbf{k})(\gamma_{\mathbf{k}\sigma}^{c+} \gamma_{\mathbf{k}\sigma}^c - \gamma_{\mathbf{k}\sigma}^{v+} \gamma_{\mathbf{k}\sigma}^v) \quad . \tag{5}$$

Here $\gamma_{\mathbf{k}\sigma}^{c(+)}, \gamma_{\mathbf{k}\sigma}^{v(+)}$ destroy (create) quasi particles in the SDW conduction and valence band, respectively. The primed summation is restricted to momenta in the magnetic Brillouin zone (MBZ), i.e. to the momenta of the occupied Fermi sea for the non interacting system ($\varepsilon(\mathbf{k}) < 0$), and the quasi particle energy dispersion is given by

$$E(\mathbf{k}) = \sqrt{\varepsilon^2(\mathbf{k}) + \Delta^2} \ . \tag{6}$$

The SDW energy gap $\Delta = UM$ between the valence and conduction band is determined from the gap equation

$$\frac{1}{N} \sum_{\mathbf{k}}{}' \frac{1}{E(\mathbf{k})} = \frac{1}{U} \tag{7}$$

and the transformation amplitudes in (4) are given by $u_{\mathbf{k}} = \sqrt{\frac{1}{2}[1 + \varepsilon(\mathbf{k})/E(\mathbf{k})]}$ and $v_{\mathbf{k}} = \sqrt{\frac{1}{2}[1 - \varepsilon(\mathbf{k})/E(\mathbf{k})]}$.

Due to magnetic umklapp scattering from the periodic SDW potential the single particle propagator is no longer momentum diagonal and it is conveniently expressed as a 2×2 matrix with respect to the momenta $\mathbf{q} \in$ MBZ and $\mathbf{q}+\mathbf{Q}$. In this notation the Hartree Fock c-particle propagator in the SDW state is written as

$$\mathbf{G}_0^\sigma(\mathbf{k};\omega) = \begin{pmatrix} \omega + \varepsilon(\mathbf{k}) & \sigma\Delta \\ \sigma\Delta & \omega - \varepsilon(\mathbf{k}) \end{pmatrix} \frac{1}{\omega^2 - E^2(\mathbf{k}) + i\delta} \quad . \tag{8}$$

Alternatively we will in subsequent chapters also use the diagonal propagator matrix for the SDW conduction and valence band quasi particles. The transformation between the c and γ representation for the propagator matrices reads

$$\mathbf{G}_0^\sigma(\mathbf{k};\omega) = \mathbf{U}^+(\mathbf{k},\sigma)\mathbf{G}^\gamma(\mathbf{k},\omega)\mathbf{U}(\mathbf{k},\sigma) \tag{9}$$

with

$$\mathbf{G}^\gamma(\mathbf{k};\omega) = \begin{pmatrix} G_\gamma^c & 0 \\ 0 & G_\gamma^v \end{pmatrix}$$
$$= \begin{pmatrix} \dfrac{1}{\omega - E(\mathbf{k}) + i\delta} & 0 \\ 0 & \dfrac{1}{\omega + E(\mathbf{k}) - i\delta} \end{pmatrix} \quad . \tag{10}$$

The collective spin wave excitations in the SDW state are determined by the poles of the frequency Fourier transform of the transverse susceptibilities

$$\chi^{\sigma,-\sigma}(\mathbf{q},\mathbf{q}\,';t) = \frac{i}{2N} \langle\psi|TS_{\mathbf{q}}^\sigma(t)S_{-\mathbf{q}'}^{-\sigma}(0)|\psi\rangle \ , \tag{11}$$

where here $\sigma = \pm$. The local spin raising and lowering operators $S_j^\sigma = S_j^x + \sigma i S_j^y$ are represented in terms of fermion operators by

$$S_j^\mu = \frac{1}{2}\sum_{\alpha\beta} c_{\alpha j}^+ \sigma_{\alpha\beta}^\mu c_{\beta j} \ , \tag{12}$$

where σ^μ denotes the Pauli matrices with $\mu = x, y$. In the following we denote by $\boldsymbol{\chi}(\mathbf{q})$ 2×2 matrices as in (8).

For the calculation of the dynamic transverse susceptibility matrix we account for the residual interactions between the quasi particles beyond the mean field approximation by summing the standard (RPA) ladder diagram series [16]. This leads to the matrix equation:

$$\boldsymbol{\chi}_{RPA}^{\sigma,-\sigma}(\mathbf{q};\omega) = \boldsymbol{\chi}_0^{\sigma,-\sigma}(\mathbf{q};\omega)\left[1 - U\boldsymbol{\chi}_0^{\sigma,-\sigma}(\mathbf{q};\omega)\right]^{-1} \ , \tag{13}$$

with

$$\boldsymbol{\chi}_0^{\sigma,-\sigma}(\mathbf{q};\omega) = \frac{1}{N}\sum_{\mathbf{k}}{}' \begin{pmatrix} m_{\mathbf{k},\mathbf{k}+\mathbf{q}}^2 & \sigma l_{\mathbf{k},\mathbf{k}+\mathbf{q}}m_{\mathbf{k},\mathbf{k}+\mathbf{q}} \\ \sigma l_{\mathbf{k},\mathbf{k}+\mathbf{q}}m_{\mathbf{k},\mathbf{k}+\mathbf{q}} & l_{\mathbf{k},\mathbf{k}+\mathbf{q}}^2 \end{pmatrix}$$
$$\times \left[\frac{1}{\omega + E(\mathbf{k}) + E(\mathbf{k}+\mathbf{q}) - i\delta} \right.$$
$$\left. \pm \frac{1}{\omega - E(\mathbf{k}) - E(\mathbf{k}+\mathbf{q}) + i\delta} \right] \tag{14}$$

and the coherence factors

$$l_{\mathbf{k},\mathbf{k}+\mathbf{q}} = u_{\mathbf{k}}u_{\mathbf{k}+\mathbf{q}} + v_{\mathbf{k}}v_{\mathbf{k}+\mathbf{q}} \ , \quad m_{\mathbf{k},\mathbf{k}+\mathbf{q}} = u_{\mathbf{k}}v_{\mathbf{k}+\mathbf{q}} + v_{\mathbf{k}}u_{\mathbf{k}+\mathbf{q}} \ . \tag{15}$$

In (14) the upper (lower) sign refers to the off-diagonal (diagonal) matrix elements, respectively. The spin wave dispersion $\omega_{sw}(\mathbf{q})$ follows from the condition $\det[1 - U\boldsymbol{\chi}^{+-}(\mathbf{q};\omega)] = 0$. In the strong coupling limit $U \gg t$ the RPA susceptibility matrix takes a very transparent form displaying explicitly the propagating spin wave excitations. An expansion of $\chi_{RPA}^{\sigma,-\sigma}$ up to the second order in t/U and ω/U leads to [17]

$$\boldsymbol{\chi}_{sc}^{\sigma,-\sigma}(\mathbf{q};\omega) = \begin{bmatrix} -2J\left(1 - \gamma_{\mathbf{q}}\right) & \sigma\omega \\ \sigma\omega & -2J\left(1 + \gamma_{\mathbf{q}}\right) \end{bmatrix}$$
$$\times \frac{1}{\omega^2 - \omega_{sw}^2(\mathbf{q}) + i\delta} \quad . \tag{16}$$

In this strong coupling limit the spin wave dispersion $\omega_{sw}(\mathbf{q}) = 2J\sqrt{1 - (\gamma_{\mathbf{q}})^2}$ is identical to the linear spin wave (LSW) theory result of the spin $\frac{1}{2}$ Heisenberg antiferromagnet with exchange coupling $J = 4t^2/U$ [16–19].

In order to describe the coupling of the photons to the electrons we consider the Hubbard Hamiltonian in the presence of a weak transverse electromagnetic field. The Coulomb interaction of the Hamiltonian remains unchanged but the vector potential $\mathbf{A}(\mathbf{r}, t)$ of the photon field introduces a phase factor $\exp(i\int_l^j \mathbf{A}(\mathbf{r}, t) \cdot d\mathbf{r})$ into the kinetic energy. Expanding the kinetic energy part of the Hamiltonian up to second order in $\mathbf{A}$ yields[20]:

$$H_{kin} = \sum_{\mathbf{k},\sigma} \varepsilon(\mathbf{k}) c_{\mathbf{k},\sigma}^+ c_{\mathbf{k},\sigma} - \frac{e}{\hbar c} \sum_{\mathbf{q}} \mathbf{j}(\mathbf{q}) \cdot \mathbf{A}(-\mathbf{q})$$
$$+ \frac{e^2}{2\hbar^2 c^2} \frac{1}{N} \sum_{\mathbf{q}_1,\mathbf{q}_2,\alpha,\beta} A_\alpha(-\mathbf{q}_1) \tau_{\alpha\beta}(\mathbf{q}_1 + \mathbf{q}_2) A_\beta(-\mathbf{q}_2). \tag{17}$$

Here, we have introduced the current density operator $\mathbf{j}(\mathbf{q})$ with components

$$j_\alpha(\mathbf{q}) = \frac{1}{N} \sum_{\mathbf{k},\sigma} \frac{\partial \varepsilon(\mathbf{k})}{\partial k_\alpha} c_{\mathbf{k}+\mathbf{q}/2,\sigma}^+ c_{\mathbf{k}-\mathbf{q}/2,\sigma} \tag{18}$$

and the *effective* density operator

$$\tau_{\alpha\beta}(\mathbf{q}) = \frac{1}{N} \sum_{\mathbf{k},\sigma} \frac{\partial^2 \varepsilon(\mathbf{k})}{\partial k_\alpha \partial k_\beta} c_{\mathbf{k}+\mathbf{q}/2,\sigma}^+ c_{\mathbf{k}-\mathbf{q}/2,\sigma} \quad . \tag{19}$$

In second quantization the components A_α of the vector potential are expressed in terms of photon annihilation ($a_{\mathbf{q}}$) and creation ($a_{\mathbf{q}}^+$) operators by

$$A_\alpha(\mathbf{q}) = \sqrt{\frac{\hbar c^2}{\omega_{\mathbf{q}} \Omega}} \left(e_\alpha a_{-\mathbf{q}} + e_\alpha^* a_{\mathbf{q}}^+\right) \quad . \tag{20}$$

$\mathbf{e}$ is the polarisation unit vector of the photon and $\omega_{\mathbf{q}} = cq$ is the photon frequency. Since the photon wavelength for visible light frequencies is large compared to the crystal lattice spacing and to all microscopic length scales of the electronic system we can safely neglect the photon momenta and henceforth use the $q = 0$ limit for the photon field. The polarisation vectors of the commonly used experimental scattering geometries with linearly polarized light are collected in Table 1, where $\mathbf{e}_i$ and $\mathbf{e}_f$ denote the polarisation unit vectors of the incoming and scattered photon, respectively, with regard to the bonds of the CuO_2 lattice.

Table 1. Polarisation vectors for the incoming ($\mathbf{e}_i$) and scattered photon ($\mathbf{e}_f$) in the common scattering geometries

Symmetry	$\mathbf{e}_i$	$\mathbf{e}_f$
A_{1g}	$\frac{1}{\sqrt{2}}(1, 1)$	$\frac{1}{\sqrt{2}}(1, 1)$
B_{1g}	$\frac{1}{\sqrt{2}}(1, 1)$	$\frac{1}{\sqrt{2}}(1, -1)$
B_{2g}	$(1, 0)$	$(0, 1)$
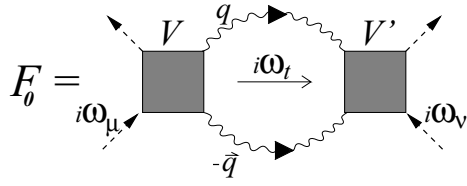
Fig. 1. General diagram for the Raman amplitude of two-magnon scattering. The dashed lines represent the incoming and outgoing photons with frequencies $i\omega_\mu, i\omega_\nu$ and the wiggly lines the magnon propagators. The vertices V and V' contain the microscopic coupling of the photons to the magnon excitations and $i\omega_t$ is the transferred photon frequency

The Hamiltonian (17) describes how the photon field couples to the current density operator and determines the bare coupling vertices for the common scattering geometries. The second order photon-electron coupling to the effective density will be neglected in the following, because it contributes to the Raman scattering intensity only at high frequencies due to direct interband transitions and does not lead to any resonance phenomena.

III. Two-magnon Raman scattering

As an alternative to the Golden Rule analysis of the Raman scattering intensity, we follow here a convenient diagrammatic formulation [21]. This method has been applied previously for calculating the Raman intensity from two-phonon scattering [22] or for two spin fluctuation scattering in the paramagnetic phase of the Hubbard model [23]. Here we extend this technique to a 2×2 matrix formulation for the SDW state. The general diagram for the Raman amplitude in the absence of magnon-magnon interactions is shown in Fig. 1. The photons couple to the electronic system through a vertex function V, creating two magnons with momenta $\mathbf{q}$ and $-\mathbf{q}$. The left side of the diagram corresponds to the physical process; the scattering intensity is then obtained from the symmetrically completed diagram by taking diagram cuts (see below) - a technique which yields results equivalent to the Golden Rule analysis. The virtue of this diagrammatic technique is that it allows to select those scattering processes which dominantly contribute to the two-magnon Raman signal [22]. Here and in the following we use the finite temperature Matsubara formalism and after analytic continuation to the real frequency axis we evaluate our results in the zero temperature limit.

The final state of interest contains two magnons with opposite momenta. Therefore the two-magnon scattering intensity can be deduced by taking a cut of the diagram for the Raman amplitude across the two magnon lines only. After analytic continuation of the photon Matsubara frequencies

the cut translates into taking the discontinuity of F_0 across the real frequency axis with respect to the transferred photon frequency $i\omega_t$,

$$I(\Delta\omega) = \frac{1}{2\pi i} \left[F_0(i\omega_t \to \Delta\omega + i\delta) - F_0(i\omega_t \to \Delta\omega - i\delta) \right] ,$$

(21)

and $I(\Delta\omega)$ is directly proportional to the scattering intensity. Explicitly, given the magnon propagators as represented by the transverse dynamic spin susceptibilities, and the vertex functions V and V', which will be calculated in Chap. IV, the Raman amplitude F_0 has the following form:

$$F_0(i\omega_t) = \frac{1}{\beta N} \sum_{\mathbf{q},\mathbf{q}',\sigma,i\omega_p} V_\sigma(\mathbf{q}, i\omega_t, i\omega_\mu, i\omega_p)\chi^{\sigma,-\sigma}(\mathbf{q}, \mathbf{q}'; i\omega_p)$$

$$\times \chi^{-\sigma,\sigma}(-\mathbf{q}, -\mathbf{q}'; i\omega_t - i\omega_p)V'_\sigma(\mathbf{q}', i\omega_t, i\omega_\nu, i\omega_p) \quad (22)$$

where β is the inverse temperature. In order to single out only the two-magnon contribution to F_0, the residues of the vertex function must be disregarded when carrying out the internal frequency sum. Similarly, the cut prescription (21) with respect to $i\omega_t$ is restricted to the arguments of the susceptibilities. (For details of this technique see [22].) The omitted high energy contributions correspond to final states with particle-hole excitations only.

The frequency sum in (22) is conveniently performed by introducing the spectral representation for the transverse dynamic spin susceptibility

$$\chi^{\sigma,-\sigma}(\mathbf{q}; i\omega_p) = -\frac{1}{\pi} \int \frac{\mathrm{Im}\chi^{\sigma,-\sigma}(\mathbf{q}; \omega + i\delta)}{i\omega_p - \omega} \mathrm{d}\omega \quad . \quad (23)$$

The analytic continuation of the Matsubara frequencies in the vertex function is performed according to the rules [22, 23]

$$i\omega_\mu \to \omega_i + i\delta$$
$$i\omega_\nu \to -\omega_i + i\delta$$
$$i\omega_t \to \omega_i - \omega_f = \Delta\omega \quad . \quad (24)$$

ω_i and ω_f are the frequencies of the incoming and outgoing photon, respectively, and $\Delta\omega = \omega_i - \omega_f$ is the photon frequency shift. Taking the cut according to (21) then yields the desired two-magnon contribution to the scattering intensity:

$$I(\Delta\omega) = \sum_{\mathbf{q},\mathbf{q}',\sigma} \frac{1}{\pi^2 N} \int \mathrm{d}\omega V_\sigma(\mathbf{q}, \Delta\omega, \omega_i + i\delta, -\omega)$$

$$\times \mathrm{Im}\chi^{\sigma,-\sigma}_{RPA}(\mathbf{q}, \mathbf{q}'; -\omega)\mathrm{Im}\chi^{-\sigma,\sigma}_{RPA}(-\mathbf{q}, -\mathbf{q}'; \Delta\omega + \omega)$$

$$\times V'_\sigma(\mathbf{q}', \Delta\omega, -\omega_i + i\delta, -\omega) \{n(\omega + \Delta\omega) - n(\omega)\} . \quad (25)$$

Here, the Bose distribution function $n(\omega)$ is evaluated in the $T \to 0$ limit. Note that V_σ and V'_σ are in fact the same vertex functions but differ in the argument for the incoming photon frequency due to the analytic continuation rules (24). As a consequence the primed vertex function $V'_\sigma(\mathbf{q})$ is equal to the complex conjugate of $V_\sigma(\mathbf{q})$. In order to outline the derivation of the scattering intensity (25) no final state magnon-magnon interactions have been included so far. The inclusion of magnon-magnon interactions will be discussed in Chap. V.
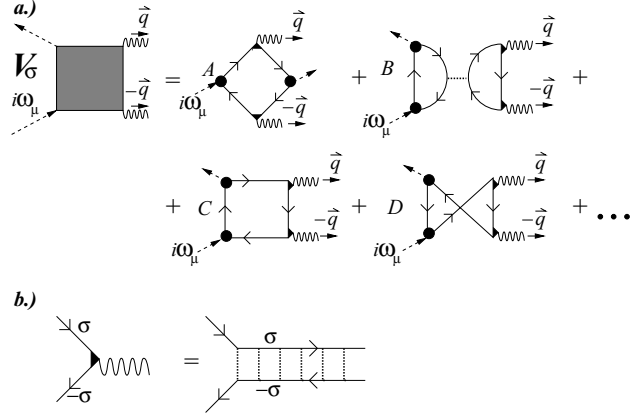
Fig. 2. a Effective vertex function for the photon-magnon coupling. The solid, dashed, and wiggly lines denote the SDW c-fermion, the photon, and the magnon propagator, respectively. The spin labeling of the fermion lines has been omitted, it is explicitly indicated in **b**. The solid circle represents the bare photon-electron coupling $\mathbf{j} \cdot \mathbf{A}$, the filled triangle represents the electron-magnon coupling where the magnons are contained in the particle-hole ladder series as shown in **b**
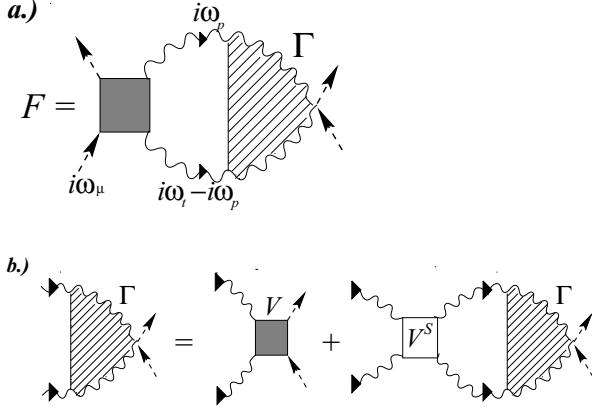
IV. The vertex function

Now we focus on the photon-magnon vertex function V_σ which depends on the incoming light frequency and is thus responsible for the resonant behavior of the scattering intensity. The electron-photon coupling Hamiltonian (17) determines the bare coupling vertices of the photon's vector potential to the current density. Given the bare photon-electron vertices the simplest and in the strong coupling limit most relevant contributions to the vertex function V_σ, which mediates the indirect coupling of the photon to the spin wave excitations, are shown by the diagrams in Fig. 2.

The algebraic expressions corresponding to the individual diagrams that contribute to the photon-magnon vertex function V_σ as shown in Fig. 2 are explicitly listed in the appendix. Since the total vertex function V_σ is independent of σ we henceforth drop the spin index σ. In addition to the diagrams shown in Fig. 2a the diagrams with reversed direction of the fermion lines have to be included as well. With (25) and the vertex function contributions as listed in the appendix the derivation of the Raman intensity in the absence of magnon-magnon interactions is complete.

V. Magnon-Magnon interaction

The remaining step is to include the effects of final state magnon-magnon interactions. From the results obtained in the framework of the Heisenberg model it is well known that it is crucial to include final state interactions in order to avoid a diverging Raman intensity at twice the maximum magnon frequency $\Delta\omega = 2\omega_{sw}^{\max} = 4J$ resulting from the square root divergence of the magnon density of states at the MBZ boundary [10–12]. We therefore extend the Raman amplitude F_0 to allow for repeated magnon-magnon scattering. This is achieved by replacing a bare vertex V in the Raman amplitude by a renormalized magnon-photon vertex function Γ which contains an infinite series of magnon pair scattering processes. Diagrammatically this is represented in

a.)

$$F = $$

b.)

$$\Gamma = V + V^S \Gamma$$

Fig. 3. a General diagram for the Raman amplitude with final state magnon-magnon interaction. **b** Diagram for the renormalized magnon-photon vertex function Γ which contains only magnon-number conserving scattering processes. The solid squares in **a** and **b** represent the bare photon-magnon coupling V (see Fig. 2) and V^S in **b** represents the irreducible magnon-magnon interaction

Fig. 3a and requires the solution of a Bethe-Salpeter like equation for Γ (see Fig. 3b). The diagrams for the Raman amplitude F and the vertex function Γ translate into the following equations:

$$F(i\omega_t, i\omega_\mu) = \frac{1}{\beta} \sum_{i\omega_p} \frac{1}{N} \sum_{\mathbf{q}_1, \mathbf{q}_1'} V(\mathbf{q}_1, i\omega_\mu, i\omega_t, i\omega_p)$$

$$\times \chi_{RPA}^{+-}(\mathbf{q}_1, \mathbf{q}_1'; i\omega_p) \chi_{RPA}^{-+}(-\mathbf{q}_1, -\mathbf{q}_1'; i\omega_t - i\omega_p)$$

$$\times \Gamma(\mathbf{q}_1', i\omega_\mu, i\omega_t, i\omega_p) \quad , \tag{26}$$

$$\Gamma(\mathbf{q}_1', i\omega_\mu, i\omega_t, i\omega_p) = V(\mathbf{q}_1', i\omega_\mu, i\omega_t, i\omega_p)$$

$$- \frac{1}{\beta} \sum_{i\omega_l} \frac{1}{N} \sum_{\mathbf{q}_2, \mathbf{q}_2'} V^s(\mathbf{q}_1', \mathbf{q}_2, i\omega_p, i\omega_t, i\omega_l) \chi_{RPA}^{+-}(\mathbf{q}_2, \mathbf{q}_2'; i\omega_l)$$

$$\times \chi_{RPA}^{-+}(-\mathbf{q}_2, -\mathbf{q}_2'; i\omega_t - i\omega_l) \Gamma(\mathbf{q}_2', i\omega_\mu, i\omega_t, i\omega_l) \quad . \tag{27}$$

For the irreducible magnon-magnon interaction V^S we include only magnon number conserving scattering processes which - at least for the Loudon-Fleury theory of Raman scattering from the Heisenberg antiferromagnet - have been shown to be the most important [24]. For our present SDW state based calculation the magnon-magnon interaction vertex has to be expressed in terms of the residual Hubbard interaction between the fermionic quasi particles. The simplest diagrams which serve for this purpose are shown in Fig. 4 and involve an internal loop with 4 fermion Green's functions. Fortunately, for our subsequent strong coupling evaluation of the two-magnon Raman intensity in B_{1g} geometry we have indeed found that these two diagrams give the dominant contribution to the magnon-magnon interaction. As we will show below, evaluating V^S in the static zero frequency limit the result for the B_{1g} intensity can still be obtained analytically for $U \gg t$ in an intermediate frequency range despite the mathematical complexity of the Raman amplitude F in (26).

$$V^S(\vec{q}_1, \vec{q}_2) = \quad + \quad$$
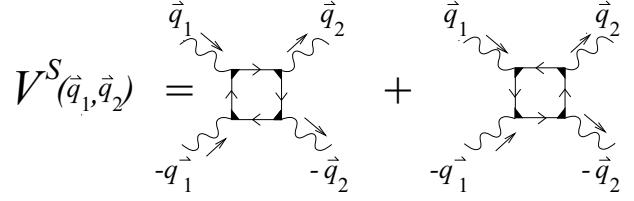
Fig. 4. Vertices for magnon-magnon scattering. As before (see Fig. 2b) the filled triangle corresponds to the electron-magnon coupling

VI. Non-resonant scattering

First we analyse the results in the non-resonant case, when the incoming photon frequency ω_i is much smaller than the SDW energy gap 2Δ. In the strong coupling limit all expressions take a transparent form and become analytically tractable. In B_{1g} symmetry the rhomb-shaped vertex diagram A in Fig. 2 gives the only contribution to the total vertex function; the diagrams B, C, and D vanish identically to leading order in t/U. Explicitly we find

$$V_A^{sc}(\mathbf{q}) = -f(\omega_i) J \gamma_{\mathbf{q}}^d \quad , \tag{28}$$

with

$$\gamma_{\mathbf{q}}^d = \frac{1}{2} \left[\cos(q_x) - \cos(q_y) \right] \quad \text{and}$$

$$f(\omega_i) \propto \frac{\Delta^2}{\omega_i^2 - 4\Delta^2} \quad . \tag{29}$$

This simple structure of the photon-magnon vertex function leads immediately to a simple expression for the scattering intensity (25) in B_{1g} geometry without final state magnon-magnon interactions:

$$I_{B_{1g}}(\Delta\omega) \propto \frac{\Delta^4}{(\omega_i^2 - 4\Delta^2)^2} \sum_{\mathbf{q}}' \frac{J^2(\gamma_{\mathbf{q}}^d)^2}{1 - \gamma_{\mathbf{q}}^2} \delta(\Delta\omega - 2\omega_{sw}(\mathbf{q})) \quad . \tag{30}$$

As expected the neglect of magnon-magnon interactions results in a logarithmic divergence of the B_{1g} intensity at twice the maximum spin wave frequency $4J$.

In A_{1g} symmetry all 4 diagrams in Fig. 2 for the vertex function give non-vanishing contributions, but due to a perfect cancellation of the different terms the total vertex function and therefore the scattering intensity vanish to leading order in t/U. This cancellation has been previously noted by Chubukov and Frenkel [15]. Also the intensity in B_{2g} symmetry is zero in the strong coupling limit. For weak and intermediate values of U/t, however, the two-magnon intensity is finite in all three symmetry channels.

The logarithmically diverging scattering intensity in B_{1g} (30) and the vanishing intensities in A_{1g} and B_{2g} symmetries for $U \gg t$ are results one also obtains using the effective Loudon-Fleury spin-photon coupling Hamiltonian in the framework of the spin $\frac{1}{2}$ Heisenberg model. In the non-resonant region, where $(2\Delta - \omega_i) \gg J$, and in the strong coupling limit the assumption of localized spins is valid and the Loudon-Fleury approach is expected to yield the correct description [15, 20]. Since we have demonstrated the equivalence between the two approaches at least in the absence of magnon-magnon interactions, the correct selection of the

photon-magnon vertex diagrams in Fig. 2 is a posteriori verified.

In order to take magnon-magnon interactions into account, we evaluate the scattering vertex V^S (see Fig. 4) in the static limit for $U \gg t$. In B_{1g} geometry the only relevant contribution to V^S is given by

$$V_{B_{1g}}^S(\mathbf{q}_1, \mathbf{q}_2) = -12 J \, \gamma_{\mathbf{q}_1 - \mathbf{q}_2} \quad . \tag{31}$$

We decompose $\gamma_{\mathbf{q}_1 - \mathbf{q}_2}$ as

$$\gamma_{\mathbf{q}_1 - \mathbf{q}_2} = \gamma_{\mathbf{q}_1} \gamma_{\mathbf{q}_2} + \gamma_{\mathbf{q}_1}^d \gamma_{\mathbf{q}_2}^d + \gamma_{\mathbf{q}_1}^{p1} \gamma_{\mathbf{q}_2}^{p1} + \gamma_{\mathbf{q}_1}^{p2} \gamma_{\mathbf{q}_2}^{p2} \quad , \tag{32}$$

where

$$\gamma_{\mathbf{q}}^{p1} = \frac{1}{2}[\sin(q_x) + \sin(q_y)] \quad \text{and}$$

$$\gamma_{\mathbf{q}}^{p2} = \frac{1}{2}[\sin(q_x) - \sin(q_y)] . \tag{33}$$

Due to the specific momentum dependence of the relevant photon-magnon vertex, (28), only the second term in (32) contributes, because in performing the momentum sum in the vertex (27) all those parts of $V_{B_{1g}}^S$ which are orthogonal to $\gamma_{\mathbf{q}}^d$ give a vanishing contribution ($\sum_{\mathbf{q}} \gamma_{\mathbf{q}}^d \gamma_{\mathbf{q}} = \sum_{\mathbf{q}} \gamma_{\mathbf{q}}^d \gamma_{\mathbf{q}}^{p1} = \sum_{\mathbf{q}} \gamma_{\mathbf{q}}^d \gamma_{\mathbf{q}}^{p2} = 0$). Therefore, the effective remaining magnon-magnon interaction V_{eff}^S in B_{1g} geometry is given by

$$V_{\text{eff}}^S(\mathbf{q}_1, \mathbf{q}_2) = -12 \, J \, \gamma_{\mathbf{q}_1}^d \gamma_{\mathbf{q}_2}^d \quad . \tag{34}$$

Introducing the function

$$L(i\omega_t) = \frac{1}{\beta} \sum_{i\omega_p} \frac{1}{N} \sum_{\mathbf{q}, \mathbf{q}'} \gamma_{\mathbf{q}}^d \chi_{SC}^{+-}(\mathbf{q}, \mathbf{q}'; i\omega_p)$$
$$\times \chi_{SC}^{-+}(-\mathbf{q}, -\mathbf{q}'; i\omega_t - i\omega_p) \gamma_{\mathbf{q}'}^d \quad , \tag{35}$$

and solving (26) and (27) with $V^S = V_{\text{eff}}^S(\mathbf{q}_1', \mathbf{q}_2)$ the B_{1g} Raman amplitude takes the form

$$F_{B_{1g}}(i\omega_t) = f^2(\omega_i) \frac{J^2 L(i\omega_t)}{1 - 12 J L(i\omega_t)} \quad . \tag{36}$$

Finally, applying the cut prescription (21) yields the result for the non-resonant scattering intensity in B_{1g} geometry

$$I_{B_{1g}}(\Delta\omega) = \frac{f^2(\omega_i)}{\pi} \text{Im} \left\{ \frac{L(\Delta\omega + i\delta)}{1 - 12 J \, L(\Delta\omega + i\delta)} \right\} \quad . \tag{37}$$

A comment is in order regarding the calculation of $L(i\omega_t)$. We note that the denominator of $\chi_{sc}^{+-}(\mathbf{q}; \omega)$ in (16) contains two poles at $\omega = \pm\omega_{sw}(\mathbf{q})$ corresponding to forward and backward propagating spin wave excitations. The vertices in Fig. 4, however, account only for magnon number conserving scattering processes. For a consistent evaluation of the Raman amplitude it is required to retain only the forward propagating parts of the dynamic susceptibilities in (35) for $L(i\omega_t)$ [25].

With this restriction for the evaluation of $L(i\omega_t)$ the resulting B_{1g} scattering intensity is shown in Fig. 5 (solid line).

As expected, the inclusion of magnon-magnon interactions removes the divergency of the intensity for zone boundary magnon pairs and leads to a single almost symmetric two-magnon peak around $\Delta\omega \cong 2.6J$. For comparison we have also shown the result of the Loudon-Fleury theory in
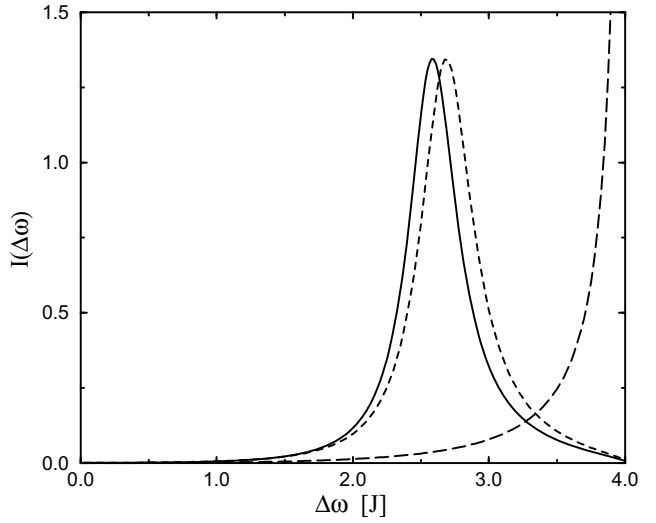
Fig. 5. Raman intensity in arbitrary units in the non-resonant case in the strong coupling limit with (solid line) and without (long dashed line) final state magnon-magnon interactions. The short dashed line shows the result of the Loudon-Fleury theory with magnon-magnon interactions included. The transferred photon frequency $\Delta\omega$ is given in units of $J = 4t^2/U$

Fig. 5 obtained from a spin wave theory analysis to order $(1/S)^2$. We note that an analogous but much more tedious expansion in the framework of the half-filled Hubbard model has been performed in [26] by extending the model to $2S$ equivalent orbitals on each site.

The line shape of the obtained spectra in Fig. 5 is apparently distinctly different from the experimental data. As we argue in this paper the reason for this discrepancy is due to the neglect of resonance phenomena in the photon-magnon vertex function V; the non-resonant limit $(2\Delta - \omega_i) \gg J$ for which the Loudon-Fleury theory is valid is not the relevant situation for the experimental Raman data on cuprate antiferromagnets.

VII. Resonant Raman scattering

In this chapter we consider the resonant case when the incoming photon frequency ω_i is comparable to the SDW energy gap to within a typical magnon energy, $(\omega_i - 2\Delta) \sim J$. In this regime strong resonant enhancement of the vertex function becomes important due to the combination of photon induced interband transitions and the creation of a magnon pair. Resonances appear in all four vertex diagrams in Fig. 2 which contribute to the total vertex function V. By inspection we find the strongest resonance to arise from a scattering process that is contained in the rhomb-shaped vertex diagram A (Fig. 2a). Alternatively to (A1) this contribution to the vertex function is more conveniently expressed in terms of SDW conduction and valence band quasi particle propagator matrices which allows more easily to identify the physical process responsible for the strongest resonance. Explicitly we rewrite the algebraic result for the diagram A as

$$V_A(\mathbf{q}, i\omega_\mu, i\omega_t, i\omega_p) = \frac{1}{\beta} \sum_{i\Omega_n} \frac{1}{N} \sum_{\mathbf{k}}{}' M_A(\mathbf{k}, \mathbf{q})$$
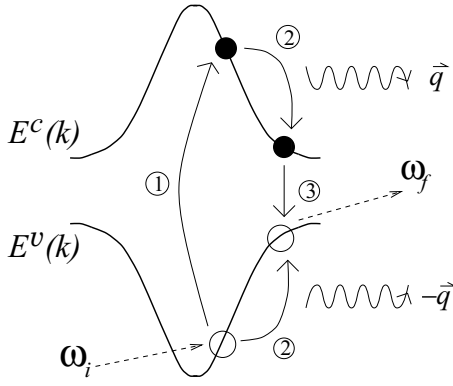
Fig. 6. Scattering process which leads to the strongest resonant enhancement of the vertex function. The dashed lines denote the incoming and outgoing photons, the wiggly lines denote the magnons. $E^v(\mathbf{k})$ and $E^c(\mathbf{k})$ mark the valence and conduction bands, respectively. *1.)* Excitation of a particle-hole pair created by absorption of the incoming photon with frequency ω_i. *2.)* Creation of a magnon pair. *3.)* Recombination of the particle-hole pair and emission of the outgoing photon with frequency ω_f

$$\times \text{Tr}[\mathbf{G}^\gamma(\mathbf{k}; i\Omega_n)\mathbf{p}(\mathbf{k}, \mathbf{k})\mathbf{G}^\gamma(\mathbf{k}, i\Omega_n + i\omega_\mu)\mathbf{p}(\mathbf{k}; \mathbf{k} - \mathbf{q})$$
$$\times \mathbf{G}^\gamma(\mathbf{k} - \mathbf{q}; i\Omega_n + i\omega_\mu - i\omega_p)\mathbf{p}(\mathbf{k} - \mathbf{q}, \mathbf{k} - \mathbf{q})$$
$$\times \mathbf{G}^\gamma(\mathbf{k} - \mathbf{q}; i\Omega_n + i\omega_t - i\omega_p)\mathbf{p}(\mathbf{k} - \mathbf{q}, \mathbf{k})] , \qquad (38)$$

where we have introduced the coherence factor matrix

$$\mathbf{p}(\mathbf{k}, \mathbf{k}') = \begin{pmatrix} n_{\mathbf{k},\mathbf{k}'} & m_{\mathbf{k},\mathbf{k}'} \\ m_{\mathbf{k},\mathbf{k}'} & -n_{\mathbf{k},\mathbf{k}'} \end{pmatrix} \qquad (39)$$

with matrix elements

$$n_{\mathbf{k},\mathbf{k}-\mathbf{q}} = u_{\mathbf{k}} v_{\mathbf{k}-\mathbf{q}} - v_{\mathbf{k}} u_{\mathbf{k}-\mathbf{q}}$$
$$m_{\mathbf{k},\mathbf{k}-\mathbf{q}} = u_{\mathbf{k}} v_{\mathbf{k}-\mathbf{q}} + v_{\mathbf{k}} u_{\mathbf{k}-\mathbf{q}} \qquad . \qquad (40)$$

The symmetry factor $M_A(\mathbf{k}, \mathbf{q})$ depends on the scattering geometry and is defined in (A5) in the appendix. Carrying out the required matrix multiplications in (38) leads to 16 combinations of conduction (G^c) and valence band propagators (G^v). Among them we single out the term which leads to the by far strongest resonant enhancement, i.e. the term containing the product $G^v G^c G^c G^v$, and neglect in the following all other combinations with weaker resonances. The physical process underlying the dominant resonance term is shown in Fig. 6. The incoming photon creates a particle-hole pair by exciting an electron from the valence into the conduction band. This initial excitation then decays into a particle-hole pair with lower energy by the creation of two magnons with zero total momentum. Finally, the particle and the hole recombine under emission of the outgoing photon. After analytic continuation the vertex function contribution of the resonant scattering process shown in Fig. 6 is given by

$$V_A^R(\mathbf{q}, \omega_i, \Delta\omega) = \frac{1}{N} \sum_{\mathbf{k}}' M_A(\mathbf{k}, \mathbf{q}) \frac{m_{\mathbf{k},\mathbf{k}}}{(\omega_i - 2E(\mathbf{k}) + i\delta)} \qquad (41)$$

$$\times \frac{n_{\mathbf{k},\mathbf{k}-\mathbf{q}} \, m_{\mathbf{k}-\mathbf{q},\mathbf{k}} \, n_{\mathbf{k}-\mathbf{q},\mathbf{k}-\mathbf{q}}}{(\omega_i - \frac{\Delta\omega}{2} - E(\mathbf{k}) - E(\mathbf{k}-\mathbf{q}) + i\delta)(\omega_i - \Delta\omega - 2E(\mathbf{k}-\mathbf{q}) + i\delta)} .$$

Here we have already identified $\Delta\omega = \omega_i - \omega_f = 2\omega_{sw}(\mathbf{q})$ as enforced by the energy conserving δ-functions contained in the imaginary parts of the transverse dynamic susceptibilities [see (16)]. The strong resonant enhancement of the vertex
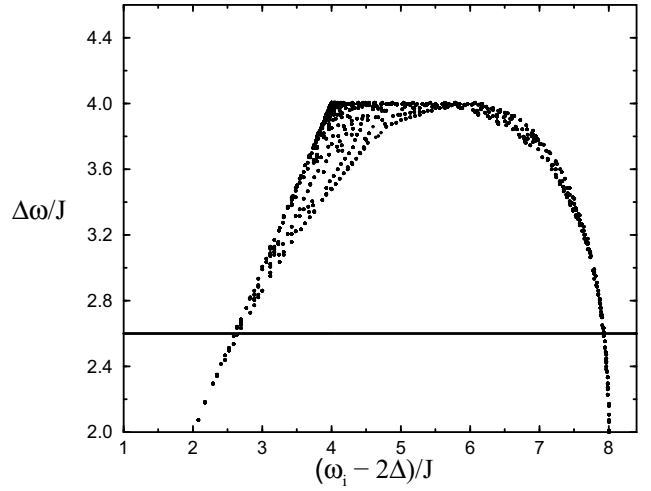
Fig. 7. Numerical solution of the triple resonance conditions. Each point in the figure corresponds to a pair $(\omega_i - 2\Delta, \Delta\omega)$ where momenta $\mathbf{k}$ and $\mathbf{q}$ exist so that the resonance conditions are simultaneously fulfilled. The solid line marks the position of the two-magnon peak in the non-resonant case

part V_A^R results from the possible simultaneous vanishing of its three energy denominators and has therefore been termed a "triple resonance" in [15]. A triple resonance occurs if the following conditions hold:

$$\omega_i = 2E(\mathbf{k}) \quad , \quad \omega_i - \Delta\omega = 2E(\mathbf{k} - \mathbf{q}) \quad . \qquad (42)$$

The triple resonance conditions have been studied in detail analytically in [15] by Chubukov and Frenkel. We have confirmed their results by solving numerically the triple resonance equations for ω_i and $\Delta\omega$ for a sequence of magnon momenta $\mathbf{q}$ in the MBZ. The numerical results are shown in Fig. 7 together with the position of the two-magnon peak in the non-resonant case. The boundary of the triple resonance region, i.e. the region in the $(\omega_i, \Delta\omega)$ plane, where the resonance conditions can be matched, is determined by the high symmetry directions in the MBZ. Each point in the figure corresponds to a magnon momentum $\mathbf{q}$ and marks the frequencies $\Delta\omega$, ω_i for which the triple resonance equations (42) can be solved for electronic momenta $\mathbf{k}$ in the MBZ. The vertex function V_A^R diverges for those values of ω_i and $\Delta\omega$, which lie in the indicated region (Fig. 7) (as long as quasi particle lifetime effects are neglected).

In our slightly different calculational scheme we have so far reconfirmed the results of Chubukov and Frenkel for the location of the divergency of the vertex function arising from the vanishing of the denominators in (41). The obvious important task is now to explore the change of the two-magnon Raman intensity profile due to the triple resonance vertex function.

In the non-resonant case we essentially exploited the $\gamma_{\mathbf{q}}^d$ momentum dependence of the photon-magnon vertex function in the strong coupling limit for the calculation of the scattering intensity in B_{1g} geometry. In this case the $\gamma_{\mathbf{q}}^d$ momentum dependence arises simply from the B_{1g} symmetry factor $M_A(\mathbf{k}, \mathbf{q})$ and from neglecting the momentum dependence of the SDW quasi particle propagators to leading order in t/U. In the present case the symmetry factor is left unchanged but the structure of the resonant vertex function

modifies the momentum dependence of $V_A(\mathbf{q})$. Nevertheless, numerical calculations show that for intermediate photon frequencies $3 < (\omega_i - 2\Delta)/J < 5$ the $\mathbf{q}$-dependence of V_A^R in B_{1g} geometry still follows very closely the $\gamma_{\mathbf{q}}^d$ form. In order to solve the Bethe-Salpeter equation for the renormalized vertex Γ even with a triple resonant photon-magnon vertex function we project V_A^R on the $\gamma_{\mathbf{q}}^d$-channel, i.e. we single out the $\gamma_{\mathbf{q}}^d$ symmetry component of V_A^R by introducing

$$\tilde{V}_A^R(\mathbf{q}, \omega_i, \Delta\omega) = g(\omega_i, \Delta\omega)\, \gamma_{\mathbf{q}}^d \qquad , \tag{43}$$

where

$$g(\omega_i, \Delta\omega) = \frac{\sum_{\mathbf{q}}' \gamma_{\mathbf{q}}^d V_A^R(\mathbf{q}, \omega_i, \Delta\omega)}{\sum_{\mathbf{q}}' \left(\gamma_{\mathbf{q}}^d\right)^2} \qquad . \tag{44}$$

Using the projection $\tilde{V}_A^R$ of the triple resonance vertex term instead of V_A^R the calculation of the B_{1g} scattering intensity proceeds completely analogous to Chap. VI and leads to

$$I_{B_{1g}}(\Delta\omega) = \frac{1}{\pi} |g(\omega_i, \Delta\omega)|^2 \,\mathrm{Im}\left\{\frac{L(\Delta\omega + i\delta)}{1 - 12J\,L(\Delta\omega + i\delta)}\right\}. \tag{45}$$

The result for the resonant B_{1g} Raman intensity thus factorizes into the absolute square of the $\gamma_{\mathbf{q}}^d$ symmetry component of the vertex function and the two-magnon part which remains unchanged. The spectrum therefore consists of two separate contributions of distinct origin: the two-magnon peak at $\Delta\omega \approx 2.6J$ and the triple resonance peak which appears well above the two-magnon peak close below $4J$ for an intermediate photon frequency range $3 < (\omega_i - 2\Delta)/J < 5$ (see Fig. 7).

Clearly, the magnitude of the triple resonance structure in the two-magnon intensity profile depends on the strength of the quasi particle damping resulting from self-energy corrections due to residual interactions between the SDW quasi particles [27]. Similarly, its precise location depends on the renormalized band dispersion. Here, for the purpose of demonstrating the consequence of the triple resonance vertex on the two-magnon line shape, we model the effect of quasi particle damping by adding a finite imaginary part to the energy denominators of the triple resonant vertex function. For the choice of a typical quasi particle lifetime we are guided by the results of a self-consistent non-crossing calculation of the self-energy correction in the SDW state of the half-filled Hubbard model [27]. The result for the two-magnon intensity in B_{1g} geometry with magnon-magnon interactions and a broadened triple resonance vertex function is shown in Fig. 8.

VIII. Discussion

Figure 8 shows a comparison of our result for the two-magnon Raman intensity in B_{1g} geometry to the experimental spectrum for La_2CuO_4 taken from [4]. In order to isolate the two-magnon signal a background was substracted from the experimental data as in [31]. The calculated lineshape is dominated by the two-magnon peak but its high energy shoulder results solely from the triple resonance enhancement in the photon-magnon vertex function. The charge transfer energy gap in La_2CuO_4 is about 2 eV as deduced

a)

b)
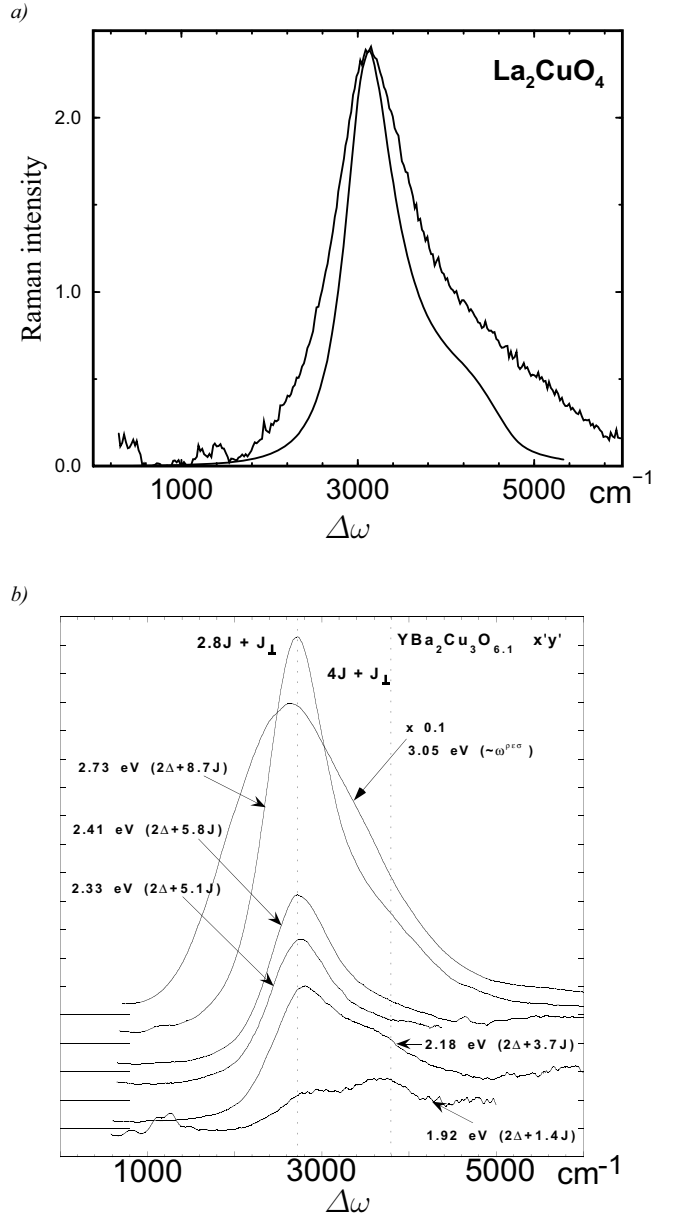
Fig. 8. a Raman scattering intensity in arbitrary units in B_{1g} geometry as calculated from (45) with $(\omega_i - 2\Delta) = 3.6J$ for a lattice with 100×100 sites. For the two-magnon term an imaginary broadening of $i\delta = i0.09J$ was used in the frequency denominators, while the vertex part was evaluated with $\delta = 0.4J$. The jagged line displays the experimental spectrum of La_2CuO_4 taken at room temperature with a laser frequency of $\omega_i = 2.55$ eV [4]. As in [31] a background was substracted from the Raman data. For comparison with the data the magnetic energy scale was set to $J = 1200$ cm^{-1} and the peak intensities were scaled to coincide. **b** Experimental spectra of $YBa_2Cu_3O_{6.1}$ at $T = 5$ K for various laser energies as indicated in the figure (reproduced from [29])

from measurements of the optical conductivity [28]. So for the laser photon frequency $\omega_i = 2.55$ eV used in the Raman experiment we have $\omega_i - 2\Delta \sim 550$ meV. For the calculation of the Raman intensity we chose $J = 1200$ cm^{-1} such that the two-magnon peak frequency coincides with the experimental value and $\omega_i - 2\Delta = 3.6J \sim 550$ meV. For intermediate photon frequencies $(\omega_i - 2\Delta) \sim 4J$ we obtain a lineshape that is in fair agreement with the experimental

spectra not only for La_2CuO_4 but also for the AF double-layer compound $YBa_2Cu_3O_{6.1}$ near resonance as shown in Fig. 8b for a series of photon frequencies [29].

Besides the high energy shoulder other experimental features in the scattering intensity find a natural explanation as well by the interplay between the two-magnon peak and the triple resonance:

(a) Two separate resonance frequencies

Recent measurements of the Raman intensity by Blumberg et al. [29] show an enhancement of the absolute Raman intensity for two different, well separated photon frequencies ω_i. In our analysis the Raman intensity as a function of ω_i is expected to increase if the frequencies for the two-magnon and the triple resonance peak merge. This does, in fact, happen for two distinct frequencies $(\omega_i - 2\Delta) \approx 2.6J$ and $(\omega_i - 2\Delta) \approx 8J$. These frequencies can be read off from Fig. 7 from the intersections of the two-magnon peak frequency (horizontal line) with the triple resonance region.

(b) $\omega_i^{res} > 2\Delta$

The same arguments as in (a) apply also for understanding the experimental observation that resonance occurs for incoming photon frequencies well above the insulating energy gap 2Δ. This has already been pointed out previously in [29].

(c) Changing line shape

The experimental spectra in Fig. 8b show a decreasing asymmetry with increasing photon frequency ω_i. The two spectra for $YBa_2Cu_3O_{6.1}$ taken at the lowest frequencies contain two well separated contributions, whereas the total line shape of the spectrum of the largest laser frequency is nearly symmetric and the two peaks are indistinguishable. (For a detailed discussion of these spectra see [30].) Within our calculation, the almost symmetric intensity profile corresponds to the near coincidence of the triple resonance and the two-magnon peak frequencies.

Figure 8 a shows Raman data of La_2CuO_4, which were taken at room temperature [4]. The most noticeable difference to the calculated intensity is the larger peak width in the experimental spectrum. There are several possible explanations for this discrepancy. First of all one might wonder about the influence of finite temperatures, since our calculation was performed at $T = 0$. However, a comparison between the low and high temperature $(T \sim T_{Néel})$ spectra in Fig. 8a and b for La_2CuO_4 and $YBa_2Cu_3O_{6.1}$, respectively, reveals that the thermal effects are of minor importance since the spectra have a comparable peak width. Clearly, lifetime effects due to magnon-phonon and also magnon-magnon interactions in particular for the zone boundary magnons will broaden the two-magnon Raman signal. The Raman spectrum in Fig. 8a was evaluated on a 100×100 lattice and a small broadening of $i\delta = i0.09J$ in the energy denominator of the dynamic spin susceptibility was introduced only for calculational purposes. The effects of magnon-phonon and magnon-magnon interactions were neglected in the present work and the sharper peak of the calculated Raman intensity in comparison to the data is expected on physical grounds. The intention of our present analysis was, instead, to show that the resonant frequency dependence of the vertex function for the photon-magnon coupling – similar to and in

agreement with the recent work by Chubukov and Frenkel [15] – leads to a qualitative change of the two-magnon line shape and provides a natural explanation for the resonance phenomena observed in light scattering experiments on cuprate antiferromagnets.

Furthermore we neglected the contribution from four-magnon and higher order scattering processes. Canali and Girvin have attempted to include the four-magnon contribution in the framework of the Heisenberg model and the Loudon-Fleury coupling Hamiltonian [24]. Although the first three moments of the resulting scattering intensity are in good agreement with experiment and also with the series expansion results by Singh et al. [31], the experimental line shape is not successfully explained. The integrated four-magnon intensity is only 2.9% of the two-magnon intensity, and if this estimate is correct, the four-magnon contribution will barely affect the overall Raman intensity profile. Furthermore, the Canali and Girvin four-magnon peak frequency is 2.5 times larger than the two-magnon peak frequency and therefore one has to conclude that four-magnon scattering cannot be responsible for the structure in the Raman intensity near 4000 cm^{-1}.

The effects of phonon-magnon interaction have been studied previously in [32–34] for Raman scattering in the Heisenberg antiferromagnet. As expected, the damping of zone boundary magnons does indeed lead to a significant broadening of the two-magnon signal. A qualitatively smaller contribution to the damping arises also from magnon-magnon interactions [35]. Nori et al. considered the effect of a random Gaussian variation δJ_{ij} of the exchange coupling J_0 assumed to originate from a distortion of the crystal lattice due to low frequency lattice vibrations [34]. Using numerical techniques Nori et al. showed that in this model a broad and asymmetric two-magnon line shape with an enhancement of spectral weight at higher energies emerges if the mean deviation $< \delta J_{ij} >$ is as large as $J_0/2$. Such an enormous variation of the exchange coupling, however, appears physically unreasonable. It is far from being clear whether more moderate values of $< \delta J_{ij} >$ are sufficient for this mechanism to explain the line shape of the two-magnon Raman spectra. We emphasize that in all these works [32, 33, 34] the resonant nature of the two-magnon scattering process was not taken into account.

IX. Summary and conclusions

Based on the single-band Hubbard model at half filling we have performed a microscopic analysis of two-magnon Raman scattering in a SDW antiferromagnet. In a diagrammatic formulation we have explicitly taken into account the structure of the photon-magnon coupling vertex. This allows to explore both, the non-resonant $(\omega_i \ll 2\Delta)$ and the resonant case $(\omega_i - 2\Delta \sim J)$ for the light scattering intensity, where the latter is the relevant limit for Raman experiments on undoped cuprate antiferromagnets. For the non-resonant case in the strong coupling limit the results of the conventional Loudon-Fleury theory for two-magnon Raman scattering in the Heisenberg antiferromagnet are almost quantitatively reproduced verifying our selection of the relevant vertex diagrams. In the resonant regime we identified the

physical process which yields the strongest diverging part of the photon-magnon vertex function and analyzed the conditions and consequences of a triple resonance. For photon frequencies well above the SDW energy gap triple resonance occurs for transferred photon frequencies larger than the two-magnon peak frequency leading to a high energy shoulder of the two-magnon intensity profile. These results confirm the conclusions of the triple resonance theory by Chubukov and Frenkel [15] for resonant two-magnon Raman scattering. In this theory effective electron-magnon vertices were constructed from the requirement that these vertices lead to the strong coupling RPA form of the transverse dynamic spin susceptibility. In contrast to the work of Chubukov and Frenkel we have performed a more systematic microscopic derivation for the two-magnon scattering intensity and we have evaluated the intensity profile by explicitly taking into account the resonant structure of the photon-magnon coupling vertex.

By using unrenormalized SDW quasi particle propagators the triple resonance leads to a true divergence of the vertex function. Self-energy corrections, however, will remove the divergence leaving a finite enhancement in the Raman intensity at the triple resonance frequency. These self-energy corrections have been calculated in previous work [27]. We have here for simplicity modelled quasi particle lifetimes effects by adding a constant damping term to the propagators in the triple resonance vertex function. A more reliable quantitative estimate for the strength of the triple resonant enhancement will require a refined treatment with the inclusion of self-energy corrections.

In conclusion, we found that the resonant frequency dependence of the photon-magnon vertex function gives rise to an enhancement of the high energy side of the two-magnon Raman peak in B_{1g} scattering geometry. The combination of resonant transitions between the SDW quasi particle bands and magnon pair excitations provides a microscopic basis for understanding the resonant Raman scattering experiments on cuprate antiferromagnets.

Appendix

For the calculation of the vertex diagrams shown in Fig. 2 we use the bare SDW single particle propagator $\mathbf{G}_0^\sigma$ (in c-fermion representation) in 2×2 matrix notation. In the finite temperature Matsubara formalism the vertex functions of the four diagrams are given explicitly by

$$V_A^\sigma(\mathbf{q}, i\omega_\mu, i\omega_t, i\omega_p) = \frac{1}{\beta} \sum_{i\Omega_n} \frac{1}{N} \sum_{\mathbf{k}}{}' M_A(\mathbf{k}, \mathbf{q})$$
$$\times \mathrm{Tr} \left[\mathbf{G}_0^\sigma(\mathbf{k}; i\Omega_n) \boldsymbol{\sigma}_z \mathbf{G}_0^\sigma(\mathbf{k}; i\Omega_n + i\omega_\mu) \right.$$
$$\times \mathbf{G}_0^{-\sigma}(\mathbf{k} - \mathbf{q}; i\Omega_n + i\omega_\mu - i\omega_p)$$
$$\left. \times \boldsymbol{\sigma}_z \mathbf{G}_0^{-\sigma}(\mathbf{k} - \mathbf{q}; i\Omega_n + i\omega_t - i\omega_p) \right] , \quad (A1)$$

$$V_B^\sigma(\mathbf{q}, i\omega_\mu, i\omega_t, i\omega_p) = \frac{1}{\beta} \sum_{i\Omega_n, i\tilde{\Omega}_n} \frac{1}{N} \sum_{\mathbf{k},\mathbf{l}}{}' M_B(\mathbf{k})$$
$$\times \mathrm{Tr} \left[\mathbf{G}_0^{-\sigma}(\mathbf{k}; i\Omega_n) \boldsymbol{\sigma}_z \mathbf{G}_0^{-\sigma}(\mathbf{k}; i\Omega_n + i\omega_\mu) \right.$$
$$\left. \times \boldsymbol{\sigma}_z \mathbf{G}_0^{-\sigma}(\mathbf{k} - \mathbf{q}; i\Omega_n + i\omega_t) \right]$$
$$\times U \, \mathrm{Tr} \left[\mathbf{G}_0^\sigma(\mathbf{l}; i\tilde{\Omega}_n) \mathbf{G}_0^\sigma(\mathbf{l}; i\tilde{\Omega}_n + i\omega_t) \right.$$
$$\left. \times \mathbf{G}_0^{-\sigma}(\mathbf{l} - \mathbf{q}; i\tilde{\Omega}_n + i\omega_t - i\omega_p) \right] , \quad (A2)$$

$$V_C^\sigma(\mathbf{q}, i\omega_\mu, i\omega_t, i\omega_p) = \frac{1}{\beta} \sum_{i\Omega_n} \frac{1}{N} \sum_{\mathbf{k}}{}' M_B(\mathbf{k})$$
$$\times \mathrm{Tr} \left[\mathbf{G}_0^\sigma(\mathbf{k}; i\Omega_n) \boldsymbol{\sigma}_z \, \mathbf{G}_0^\sigma(\mathbf{k}; i\Omega_n + i\omega_\mu) \boldsymbol{\sigma}_z \mathbf{G}_0^\sigma(\mathbf{k}; i\Omega_n + i\omega_t) \right.$$
$$\left. \times \mathbf{G}_0^{-\sigma}(\mathbf{k} - \mathbf{q}; i\Omega_n + i\omega_t - i\omega_p) \right] , \quad (A3)$$

$$V_D^\sigma(\mathbf{q}, i\omega_\mu, i\omega_t, i\omega_p) = \frac{1}{\beta} \sum_{i\Omega_n} \frac{1}{N} \sum_{\mathbf{k}}{}' M_B(\mathbf{k})$$
$$\times \mathrm{Tr} \left[\mathbf{G}_0^\sigma(\mathbf{k}; i\Omega_n) \boldsymbol{\sigma}_z \, \mathbf{G}_0^\sigma(\mathbf{k}; i\Omega_n - i\omega_\mu) \boldsymbol{\sigma}_z \mathbf{G}_0^\sigma(\mathbf{k}; i\Omega_n + i\omega_t) \right.$$
$$\left. \times \mathbf{G}_0^{-\sigma}(\mathbf{k} - \mathbf{q}; i\Omega_n + i\omega_t - i\omega_p) \right] . \quad (A4)$$

The symmetry factors of the basic scattering vertices from the coupling of the photon vector potential to the electron current density have been combined into the functions

$$M_A(\mathbf{k}, \mathbf{q}) = \frac{2\pi e^2}{\sqrt{\omega_i \omega_f} \, \Omega} \sum_{\alpha\beta} \frac{\partial \varepsilon_{\mathbf{k}}}{\partial k_\alpha} \frac{\partial \varepsilon_{\mathbf{k}+\mathbf{q}}}{\partial k_\beta} e_i^\alpha e_f^\beta , \quad (A5)$$

$$M_B(\mathbf{k}) = M_A(\mathbf{k}, \mathbf{0}) . \quad (A6)$$

Note that the factor $\partial \varepsilon_{\mathbf{k}}/\partial k_\alpha$ changes sign when umklapp scattering ($\mathbf{k} \to \mathbf{k} + \mathbf{Q}$) has taken place along the fermion lines. In the 2×2 matrix formulation the alteration of the sign is conveniently taken into account by inserting the Pauli matrix $\boldsymbol{\sigma}_z$. Including all diagrams with reversed direction of the fermion lines yields a factor two in the total vertex function.

References

1. Bednorz, J.G., Müller, K.A.: Z. Phys. B **64**, 189 (1986)
2. Vaknin, D., Sinha, S.K., Moncton, D.E., Johnston, D.C., Newsman, J.M., Safinya, C.R., King, H.E. jr.: Phys. Rev. Lett. **58**, 2802 (1987)
3. Shirane, G., Endoh, Y., Birgeneau, R.J., Kastner, M.A., Hidaka, Y., Oda, M., Suzuki, M., Murakami, T.: Phys. Rev. Lett. **59**, 1613 (1987)
4. Sulewski, P.E., Fleury, P.A., Lyons, K.B.: Phys. Rev. B **41**, 225 (1990)
5. Lyons, K.B., Fleury, P.A., Remeika, J.P., Cooper, A.S., Negran, T.J.: Phys. Rev. B **37**, 2353 (1988)
6. Lyons, K.B., Fleury, P.A., Schneemeyer, L.F., Waszczak, J.V.: Phys. Rev. Lett. **60**, 732 (1988)
7. Aeppli, G., Hayden, S.M., Mook, H.A., Fisk, Z., Cheong, S.-W., Rytz, D., Remeika, J.P., Espinosa, G.P., Cooper, A.S.: Phys. Rev. Lett. **62**, 2052 (1989)
8. Hayden, S.M., Aeppli, G., Osborn, R., Taylor, A.D., Perring, T.G., Cheong, S.-W., Fisk, Z.: Phys. Rev. Lett. **67**, 3622 (1991)
9. Itoh, S., Yamada, K., Arai, M., Endoh, Y., Hidaka, Y., Hosoya, S.: J. Phys. Soc. Jpn. **63**, 4542 (1994)
10. Fleury, P.A., Loudon, R.: Phys. Rev. **166**, 166 (1968)
11. Parkinson, J.B.: J. Phys. C **2**, 2012 (1969)
12. Elliott, R.J., Thorpe, M.F.: J. Phys. C **2**, 1630 (1969)
13. Kampf, A.P.: Phys. Rep. **249**, 219 (1994)

14. Brenig, W.: Phys. Rep. **251**, 153 (1994)
15. Chubukov, A.V., Frenkel, D.M.: Phys. Rev. Lett. **74**, 3057 (1995); Phys. Rev. B **52**, 9760 (1995);
16. Schrieffer, J.R., Wen, X.G., Zhang, S.C.: Phys. Rev. B **39**, 11663 (1989)
17. Brenig, W., Kampf, A.P.: Europhys. Lett. **24**, 679 (1993)
18. Singh, A., Tešanović, Z.: Phys. Rev. B **41**, 614 (1990)
19. Chubukov, A.V., Frenkel, D.M.: Phys. Rev. B **46**, 11884 (1992)
20. Shastry, B., Shraiman, B.: Phys. Rev. Lett. **65**, 1068 (1990); Int. J. Mod. Phys. B **5**, 365 (1991)
21. Kawabata, A.: J. Phys. Soc. Jpn. **30**, 68 (1971)
22. Klein, M.V.: Phys. Rev. B **24**, 4208 (1981)
23. Kampf, A.P., Brenig, W.: Z. Phys. B **89**, 313 (1991)
24. Canali, C.M., Girvin, S.M.: Phys. Rev. B **45**, 7121 (1992)
25. Chubukov, A.V.: private communication
26. Chubukov, A.V., Musaelian, K.A.: Phys. Rev. B **50**, 6238 (1994)
27. Altmann, J., Brenig, W., Kampf, A.P., Müller-Hartmann, E.: Phys. Rev. B **52**, 7395 (1995)
28. Uchida, S., Ido, T., Takagi, H., Arima, R., Tokura, Y., Tajima, S.: Phys. Rev. B **43**, 7942 (1991)
29. Blumberg, G., Abbamonte, P., Klein, M.V., Miller, L.L., Lee, W.C., Ginsberg, D.M.: preprint cond-mat 9511080
30. Sugai, S., Sato, M., Kobayashi, T., Akimutsu, J., Ito, T., Takagi, H., Uchida, S., Hosoya, S., Kajitani, T., Fukuda, T.: Phys. Rev. B **42**, 1045 (1990)
31. Singh, R.R.P., Fleury, K.B., Sulewski, P.E.: Phys. Rev. Lett. **62**, 2736 (1989)
32. Knoll, P., Thomson, C., Cardona, M., Murugaraj, P.: Phys. Rev. B **42**, 4842 (1990)
33. Sänger, D.U.: Phys. Rev. B **49**, 12176 (1994); Phys. Rev. B **25**, 1025 (1995)
34. Nori, F., Merlin, R., Haas, S., Sandvik, A.W., Dagotto, E.: Phys. Rev. Lett. **75**, 553 (1995)
35. Kopietz, P.: Phys. Rev. B **41**, 9228 (1990)